

# LRG-BEASTS: evidence for clouds in the transmission spectrum of HATS-46 b

E. Ahrer   P. J. Wheatley   S. Gandhi   J. Kirk   G. W. King   T. Louden   and L. Welbanks  

<sup>1</sup>Centre for Exoplanets and Habitability, University of Warwick, Gibbet Hill Road, Coventry CV4 7AL, UK

<sup>2</sup>Department of Physics, University of Warwick, Gibbet Hill Road, Coventry CV4 7AL, UK

<sup>3</sup>Leiden Observatory, Leiden University, Postbus 9513, NL-2300 RA Leiden, the Netherlands

<sup>4</sup>Center for Astrophysics | Harvard & Smithsonian, 60 Garden Street, Cambridge, MA 02138, USA

<sup>5</sup>Department of Physics, Imperial College London, Prince Consort Road, London SW7 2AZ, UK

<sup>6</sup>Department of Astronomy, University of Michigan, Ann Arbor, MI 48109, USA

<sup>7</sup>School of Earth & Space Exploration, Arizona State University, Tempe, AZ 85257, USA

Accepted 2023 March 10. Received 2023 March 3; in original form 2022 October 28

## ABSTRACT

We have performed low-resolution ground-based spectroscopy of HATS-46 b in transmission, using the EFOSC2 instrument on the ESO New Technology Telescope (NTT). HATS-46 b is a highly inflated exoplanet that is a prime target for transmission spectroscopy, having a Jupiter-like radius ( $0.95 R_{\text{Jup}}$ ) but a much lower mass ( $0.16 M_{\text{Jup}}$ ). It orbits a G-type star with a 4.7 d period, giving an equilibrium temperature of 1100 K. We observed one transit of HATS-46 b with the NTT, with the time-series spectra covering a wavelength range of 3900–9000 Å at a resolution ( $R$ ) of  $\sim 380$ . We achieved a remarkably precise transmission spectrum of  $1.03 \times$  photon noise, with a median uncertainty of 357 ppm for  $\sim 200$  Å-wide bins, despite the relative faintness of the host star with  $V_{\text{mag}} = 13.6$ . The transmission spectrum does not show strong absorption features and retrievals favour a cloudy model, ruling out a clear atmosphere with  $3.0\sigma$  confidence. We also place a conservative upper limit on the sodium abundance under the alternative scenario of a clear atmosphere. This is the eighth planet in the LRG-BEASTS (Low-Resolution Ground-Based Exoplanet Atmosphere Survey using Transmission Spectroscopy) survey, which uses 4 m-class telescopes such as the NTT to obtain low-resolution transmission spectra of hot Jupiters with precisions of around one atmospheric scale height.

**Key words:** methods: observational – techniques: spectroscopic – planets and satellites: atmospheres – planets and satellites: individual: HATS-46 b.

## 1 INTRODUCTION

The study of transit depth versus wavelength, or *transmission spectroscopy*, is an essential method to characterize the atmospheres of transiting exoplanets with both ground- and space-based telescopes (e.g. Charbonneau et al. 2002; Snellen et al. 2008; Bean, Kempton & Homeier 2010; Stevenson et al. 2014; Sing et al. 2016; May et al. 2018; Weaver et al. 2021; Alam et al. 2022; The JWST Transiting Exoplanet Community Early Release Science Team 2022). Hot Jupiters, especially those with inflated radii, are prime targets for transmission spectroscopy as they have large atmospheric scale heights due to their high temperatures, their hydrogen-dominated atmospheres, and their low surface gravities. The sample of hot Jupiters studied to date exhibits a diverse range of atmospheric properties that can include narrow or pressure-broadened sodium absorption (e.g. Fischer et al. 2016; Nikolov et al. 2018; Alam et al.

2021; McGruder et al. 2022), detections of other atomic species and/or broad molecular bands (e.g. Lendl et al. 2017; Carter et al. 2020; Ahrer et al. 2023; Alderson et al. 2023; Feinstein et al. 2023; Rustamkulov et al. 2023), Rayleigh scattering (e.g. Kirk et al. 2017; Chen et al. 2021), and sometimes super-Rayleigh slopes (e.g. Pont et al. 2013; Alderson et al. 2020; Ahrer et al. 2022), as well as high-altitude clouds muting absorption features (e.g. Gibson et al. 2013a; Knutson et al. 2014; Kreidberg et al. 2014; Lendl et al. 2016; Louden et al. 2017; Espinoza et al. 2019; Spyros et al. 2021).

Transmission spectroscopy of hot Jupiters provides crucial information about the composition and chemistry of these exoplanets to understand their formation and migration process (e.g. Öberg, Murray-Clay & Bergin 2011; Madhusudhan, Amin & Kennedy 2014; Booth et al. 2017), as well as what processes play a role in cloud and haze formation at these hot temperatures. The processes and parameters governing the presence or absence of clouds and hazes in the atmospheres of gas giants are still debated (e.g. Heng 2016; Fu et al. 2017; Fisher & Heng 2018; Pinhas et al. 2019; Gao et al. 2020).

\* E-mail: [eva-maria.ahrer@warwick.ac.uk](mailto:eva-maria.ahrer@warwick.ac.uk) (EA); [p.j.wheatley@warwick.ac.uk](mailto:p.j.wheatley@warwick.ac.uk) (PJW)

† NHFP Sagan Fellow.

**Table 1.** Parameters for the star HATS-46 and its planet HATS-46 b, with  $V_{\text{mag}}$  and spectral type as determined by Brahm et al. (2018) and all other parameters as revised by Louden & Hartman (2021).

| Parameter   | Value                         |
|---|-------------------------------|
| Stellar parameters  |                               |
| $V_{\text{mag}}$  | $13.634 \pm 0.050$            |
| Spectral type   | G                             |
| Temperature, $T_{\text{eff}}$ (K)                           | $5451 \pm 19$                 |
| Age (Gyr)   | $8.4 \pm 1.9$                 |
| Surface gravity, $\log g$ [ $\log_{10}(\text{cm s}^{-2})$ ] | $4.474 \pm 0.019$             |
| Metallicity [Fe/H]  | $-0.029 \pm 0.039$            |
| Mass ( $M_{\odot}$ )  | $0.869 \pm 0.023$             |
| Radius ( $R_{\odot}$ )                                      | $0.894 \pm 0.010$             |
| Planetary parameters  |                               |
| Period (d)  | $4.742\,3749 \pm 0.000\,0043$ |
| Mass ( $M_{\text{Jup}}$ )                                   | $0.158 \pm 0.042$             |
| Radius ( $R_{\text{Jup}}$ )                                 | $0.951 \pm 0.029$             |
| Semimajor axis (au)   | $0.052\,72 \pm 0.000\,45$     |
| Equilibrium temperature, $T_{\text{eq}}$ (K)                | $1082.1 \pm 8.2$              |
| Inclination ( $^{\circ}$ )                                  | $86.97 \pm 0.10$              |
| Surface gravity, $\log g$ [ $\log_{10}(\text{cm s}^{-2})$ ] | $2.64 \pm 0.14$               |

A larger sample size is needed to explore this parameter space, and the aim of the Low-Resolution Ground-Based Exoplanet Atmosphere Survey using Transmission Spectroscopy (LRG-BEASTS; ‘large beasts’) is to contribute to that by characterizing a large number of gaseous exoplanets in transmission at optical wavelengths. This includes the detection of hazes, Rayleigh scattering, and grey clouds in the atmospheres of WASP-52 b (Kirk et al. 2016; Louden et al. 2017), HAT-P-18 b (Kirk et al. 2017), WASP-80 b (Kirk et al. 2018), WASP-21 b (Alderson et al. 2020), and WASP-94A b (Ahrer et al. 2022), as well as detections of sodium absorption in the atmospheres of WASP-21 b (Alderson et al. 2020) and WASP-94A b (Ahrer et al. 2022). In addition, within LRG-BEASTS Kirk et al. (2019) analysed the atmosphere of WASP-39 b revealing a supersolar metallicity and Kirk et al. (2021) found tentative evidence for TiO in the atmosphere of the ultrahot Jupiter WASP-103 b.

In this paper, we present the first transmission spectrum of the exoplanet HATS-46 b. Our observations were made using the EFOSC2 instrument on the New Technology Telescope (NTT) as part of the LRG-BEASTS survey. HATS-46 b was discovered within the HATSouth survey (Bakos et al. 2013) by Brahm et al. (2018). Their photometric observations, together with follow-up radial velocity measurements, confirm HATS-46 b, which orbits its G-type host star in 4.74 d. Using *TESS* and *Gaia* data, HATS-46 b has been recharacterized by Louden & Hartman (2021), who provided revised planetary and orbital parameters: HATS-46 b has a mass of  $0.158 \pm 0.042 M_{\text{Jup}}$  and a radius of  $0.951 \pm 0.029 R_{\text{Jup}}$ , orbiting at a distance of  $0.052\,72 \pm 0.000\,45$  au; the equilibrium temperature was determined to be  $1082.1 \pm 8.2$  K. Stellar and planet parameters are summarized in Table 1. The star HATS-46 does not appear to be very active as the radial velocity measurements by Brahm et al. (2018) did not show any evidence for periodic modulation on a rotation period. Unfortunately, the signal-to-noise ratio of the radial velocity spectra was not sufficient to place constraints on the chromospheric activity from the Ca II H&K lines (Brahm et al. 2018). The *TESS* light curves showed evidence for variability, with a possible period at approximately 15 d, but if real this signal would also have been expected to be detected in the HATSouth light curve (Louden & Hartman 2021).

This paper is divided into the following sections. First, we describe the observations in Section 2, and then discuss the data reduction and analysis in Sections 3 and 4. This is followed by our discussion and conclusions in Section 5.

## 2 OBSERVATIONS

We observed HATS-46 with the NTT using the EFOSC2 instrument (Buzzoni et al. 1984) on the night of 2017 August 17.<sup>1</sup> EFOSC2 is mounted at the Nasmyth B focus of the ESO NTT in La Silla, Chile, which has a Loral/Lesser CCD detector with a size of  $2048 \times 2048$  pixels. The overall field of view is 4.1 arcmin with a resolution of 0.12 arcsec per pixel and a pixel binning of  $2 \times 2$  was applied.

At our request, a slit with a width of 27 arcsec was custom-built, with the aim of avoiding differential slit losses between target and comparison stars. Grism #13 was used for our spectroscopic measurements, providing a low-resolution ( $R \sim 380$ ) spectrum from 3900 to 9000 Å.

In total, 93 spectral frames were acquired, each with a relatively long exposure time of 240 s due to the relatively faint magnitude of both target and comparison stars. The read-out time was 22 s. The observations were taken at an airmass ranging from 1.60 to 1.12 to 1.26. The illumination of the moon was at 16 per cent and it only rose towards the very end of the observation night at a distance to the target of  $108^{\circ}$ .

For calibration, 67 bias frames were acquired, as well as 112 flat frames (54 lamps, 53 skies, and 5 domes) and 3 HeAr arc frames, taken at the beginning of the night. While we experimented with using flat frames in our data reduction, we did not use any in our final reduction as we found it to increase the noise in our data. This is in line with previous reports of similar analyses, by both the LRG-BEASTS and the Atmospheric Characterization Collaboration for Exoplanet Spectroscopic Studies (ACCESS) surveys (e.g. Rackham et al. 2017; Bixel et al. 2019; Weaver et al. 2020; Kirk et al. 2021).

A nearby star (UCAC4 169-000364) at a distance of 1 arcmin to the target star HATS-46 served as a comparison star and is not known to be a variable star. The two stars are a good match in both magnitude ( $\Delta V_{\text{mag}} = 0.87$ ) and colour [ $\Delta(B - V) = 0.09$ ], thus well suited for differential spectrophotometry.

## 3 DATA REDUCTION

LRG-BEASTS observations are commonly reduced using a custom-built PYTHON pipeline, which is described in detail by Kirk et al. (2018). The data for HATS-46 have been reduced following this pipeline, but with modifications to the cosmic ray removal and wavelength calibration, introduced in Ahrer et al. (2022). In the following, we summarize the reduction steps.

First, the biases were median combined to produce a master bias. When executing the PYTHONscript for extracting the spectra from each science frame, the master bias is subtracted from each science frame. However, before extracting the spectra from the individual frames, pixels affected by cosmic rays were identified and replaced with the median of the surrounding pixels.

An aperture width of 32 pixels was applied to extract the spectral counts from each star. To fit the sky background, we used a second-order polynomial, which was fitted to regions of 50 pixels on either

<sup>1</sup>Based on observations collected at the European Organisation for Astronomical Research in the Southern Hemisphere under ESO programme 099.C-0390(A) (PI: Kirk).

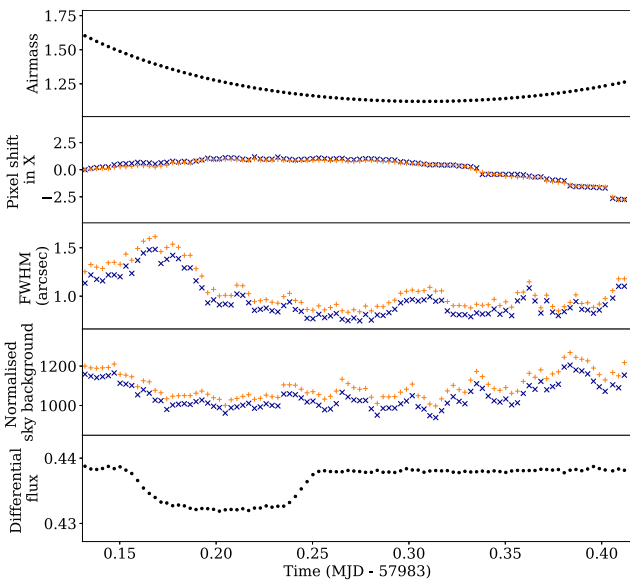


**Figure 1.** From top to bottom: variations of airmass, pixel shift along the X-axis, FWHM, sky background, and differential flux across the night. In the middle panels, the target is indicated with dark blue X symbols, and the comparison star with orange + symbols.

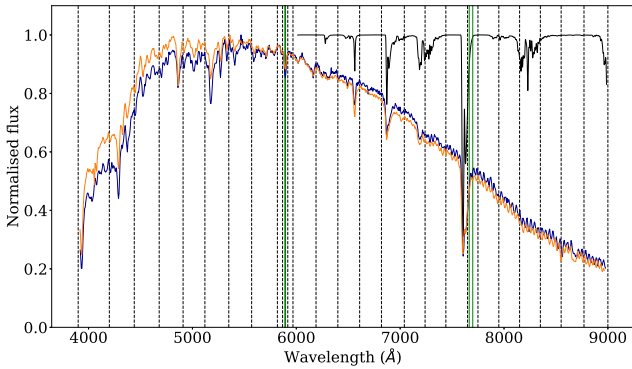


**Figure 2.** Normalized spectra of comparison star (orange) and target star (dark blue), as well as the expected strong telluric lines (black) in the redder part of the wavelength range. Wavelength bin edges are indicated with dashed black lines. Green lines indicate the position of the sodium doublet (5890, 5895 Å) and potassium doublet (7665, 7699 Å).

side of the stars at a distance of 5 pixels from the edge of the aperture. Outliers of more than three standard deviations were masked from the fit. Extracted properties such as airmass, pixel shift along the slit, full width at half-maximum (FWHM), normalized sky background, and differential white-light flux and their changes throughout the night are displayed in Fig. 1. Example spectra are plotted in Fig. 2.

Wavelength calibration follows the spectral extractions and is a two-step process. First, RASCAL (Veitch-Michaelis & Lam 2019) was utilized to find a wavelength solution using the HeAr arc frames. The second step is to optimize the wavelength calibration by fitting the positions of the stellar absorption lines in each frame, adjusting the solution, and then saving the wavelength solution for each frame individually. This allowed us to account for wavelength drifts between the frames throughout the night, which were of the order of  $\sim 5$  pixels or  $\sim 20$  Å.

Lastly, the spectra were binned into 26 wavelength bins, computed by summing the flux within the corresponding wavelength range of

each frame and dividing by the comparison star’s flux in the same wavelength bin to correct for the effects of the Earth’s atmosphere. Similarly, a white-light light curve was computed by defining one single bin across the whole wavelength range. Bin widths of  $\sim 200$  Å (avoiding edges of strong stellar absorption lines) were applied across the whole spectral range, with the exception of two small ranges where we searched for absorption by sodium and potassium, see Fig. 2.

Observations with EFOSC2 at wavelengths  $> 7200$  Å are subject to fringing effects (see Fig. 2). We found that correcting for these effects in the individual spectra using flat fields was not possible as the fringing changed in amplitude and phase during the night and the acquired flat frames were taken before the observations started.

## 4 DATA ANALYSIS

### 4.1 Transit model

Each transit light curve was described using the BATMAN PYTHON package (Kreidberg 2015) in combination with the analytic light curves from Mandel & Agol (2002) and fitted using the nested sampling algorithm POLYCHORD (Handley, Hobson & Lasenby 2015). First, the white-light light curve was fitted using the ratio of planet-to-star radius  $R_p/R_*$ , the inclination of the system  $i$ , the scaled stellar radius  $a/R_*$ , the time of mid-transit  $T_C$ , and the two quadratic limb-darkening coefficients  $u1$  and  $u2$ . We computed the limb-darkening coefficients with the Limb-Darkening Toolkit (LDTK) package (Parviainen & Aigrain 2015), which uses PHOENIX models (Husser et al. 2013) based on the stellar parameters to determine  $u1$  and  $u2$  and their errors. One of them ( $u2$ ) was held fixed to the generated value to avoid degeneracy, while the other one was fitted for ( $u1$ ) using a uniform prior with four times the generated error (see Table 2) to allow for small inconsistencies between the stellar model and the observation. This quadratic limb-darkening law provides a good fit to the data, see Section 4.2, and the fitted values for  $u1$  were consistent with the model prediction. The Kipping parametrization (Kipping 2013) was also tested to check for potential effects in the transmission spectrum due to the chosen limb-darkening parametrization, but we can confirm that this is not the case.

All priors for the system parameters can be found in Table 2, which were chosen to be uniform and wide ( $\pm 5\sigma$ ) centred on the previously reported literature values (Table 1; Louden & Hartman 2021). Depending on the detrending method, additional parameters were added to the fitting (introduced in the following section).

The determined values for  $a/R_*$ ,  $i$ , and  $T_C$  from the white-light light-curve fitting (Table 2) were then held fixed for the spectroscopic light-curve fitting, which allowed us to fit for relative changes in transit depths over the wavelength range. Thus, the fitting parameters for each of the 26 binned light curves were transit depth  $R_p/R_*$ , limb-darkening coefficient  $u1$ , and additional noise modelling parameters.

### 4.2 Light-curve fitting

For detrending the white-light light curve, various different approaches were investigated e.g. different combinations of kernels and kernel inputs for a Gaussian Process (GP), first- and second-order polynomials using airmass, FWHM, derotator angle, etc. However, all of these models retrieved very low amplitudes for their respective noise modelling, e.g. see amplitude of the best-fitting GP model in top panel in Fig. 3 which is 0.062 per cent compared to the transit depth of 1.287 per cent. In addition, the Bayesian evidence values for each of these fits did not statistically favour a particular GP model

**Table 2.** Parameter values obtained from the white-light light-curve fitting and the respective priors. Values for semimajor axis  $a$ , radius of the star  $R_*$ , radius of the planet  $R_p$ , and inclination  $i$  are listed in Table 1. The retrieved values for the parameters  $a/R_*$ ,  $i$ , and  $T_C$  listed here were fixed for the spectroscopic light-curve fitting.

| Parameter                         | Prior distribution and range | Fitted values  |
|-----------------------------------|------------------------------|--|
| Scaled stellar radius ( $a/R_*$ ) | Uniform                      | $a/R_* \pm 5\sigma_{a/R_*}$ $13.94^{+0.24}_{-0.65}$                            |
| Inclination, $i$ ( $^\circ$ )     | Uniform                      | $i \pm 5\sigma_i$ $87.60^{+0.12}_{-0.33}$                                      |
| Time of mid-transit, $T_C$ (BJD)  | Uniform                      | $0.9 \times T_C, 1.1 \times T_C$ $2457\,983.707\,25^{+0.000\,46}_{-0.000\,33}$ |
| Transit depth ( $R_p/R_*$ )       | Uniform                      | $R_p/R_* \pm 5\sigma_{R_p/R_*}$ $0.112\,50^{+0.000\,18}_{-0.000\,83}$          |
| Limb-darkening coefficient, $u1$  | Uniform                      | $u1 \pm 4\sigma_{u1}$ $0.547 \pm 0.014$  |
| Limb-darkening coefficient, $u2$  | Fixed                        | — $0.1171$   |

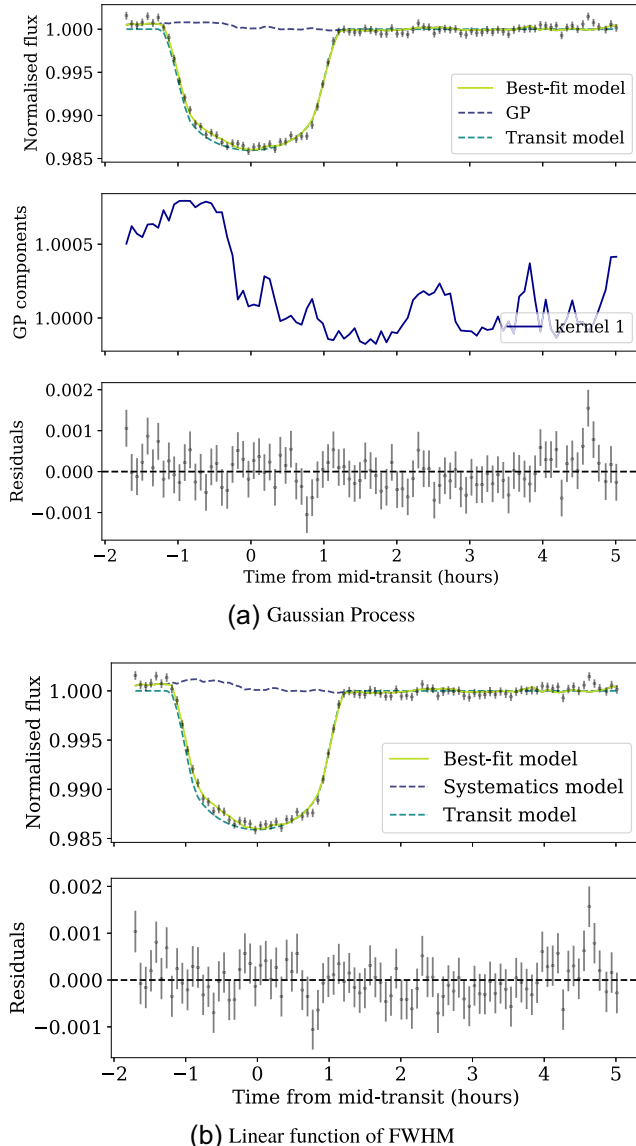


**Figure 3.** The white-light light curve fitted with a transit and two different models to account for systematics. The best-fitting model is plotted in green, while the individual components of the model are plotted in dashed turquoise for the transit model, and dark blue for the respective systematics models. In the top panels, labelled (a), we use a GP model for systematics. In the lower panels, labelled (b), we use a linear function of FWHM.

or parametric fitting model. The differences across all wavelengths in Bayesian evidences averaged at 0.5 ( $0.67\sigma$ ) and never exceeded 1 ( $<1.15\sigma$ ). Consequently, we opted to use only a linear dependence on the FWHM for detrending the white-light light curve, see bottom panel in Fig. 3.

To determine the transit depths for each wavelength bin, we fitted the individual light curves of the 26 bins with a transit model and a detrending model. We conducted an investigation of the systematics modelling, similar to the one done for the white-light light-curve fit. This was to ensure that our transmission spectrum is independent of the choice of noise modelling, and to provide the best estimate of the uncertainties.

The light curves show very little evidence for systematic trends such as drifts or correlated noise, see left-hand panel in Fig. 4 for the raw light curves. We experimented with simple models to account for the small noise amplitudes, as well as using a transit model without any systematic modelling at all. First, linear models in time, airmass, and FWHM were investigated, with the linear in FWHM performing the best according to the Bayesian evidence value of each spectroscopic light-curve fit and an average fitted noise amplitude of 0.06 per cent or 600 ppm. In addition, we looked into GP models and sampled different types of kernels and kernel input, out of which the exponential-squared model with FWHM as input resulted in the best choice, with an average fitted GP amplitude of 0.03 per cent or 300 ppm. As both, the linear in FWHM and GP model resulted in similar transit depths and small noise amplitudes, we chose the first, parametric model over the GP model due to its lower uncertainties in the transit depths. This results in an average precision of transit depth error equal to  $1.03 \times$  photon noise. The light curves and respective fits are shown in Fig. 4, as well as the residual scatter of the fits and their respective root mean square (RMS) values.

The previously described models all favoured only small variations and FWHM as the detrending source for all spectroscopic bins. This led us to investigate using a common noise model (e.g. as used in Sing et al. 2012; Gibson et al. 2013b; Lendl et al. 2016; Nikolov et al. 2016; Nortmann et al. 2016; Huitson et al. 2017; Todorov et al. 2019; Wilson et al. 2020; Kirk et al. 2021; McGruder et al. 2022) in the hope of reducing our uncertainties and getting rid of common noise structures potentially dominating the systematics. In this method the GP component from the white-light light-curve fit is subtracted from the spectroscopic light curves before fitting them individually. However, this did not have the desired effect of improving the noise modelling and on average resulted in larger uncertainties. Therefore, we did not pursue this method further.

All computed transmission spectra using the GP model, the polynomial model, the common noise model, and one without any detrending at all i.e. solely a transit model, are shown in Fig. 5. This demonstrates that our resulting transmission spectrum is independent

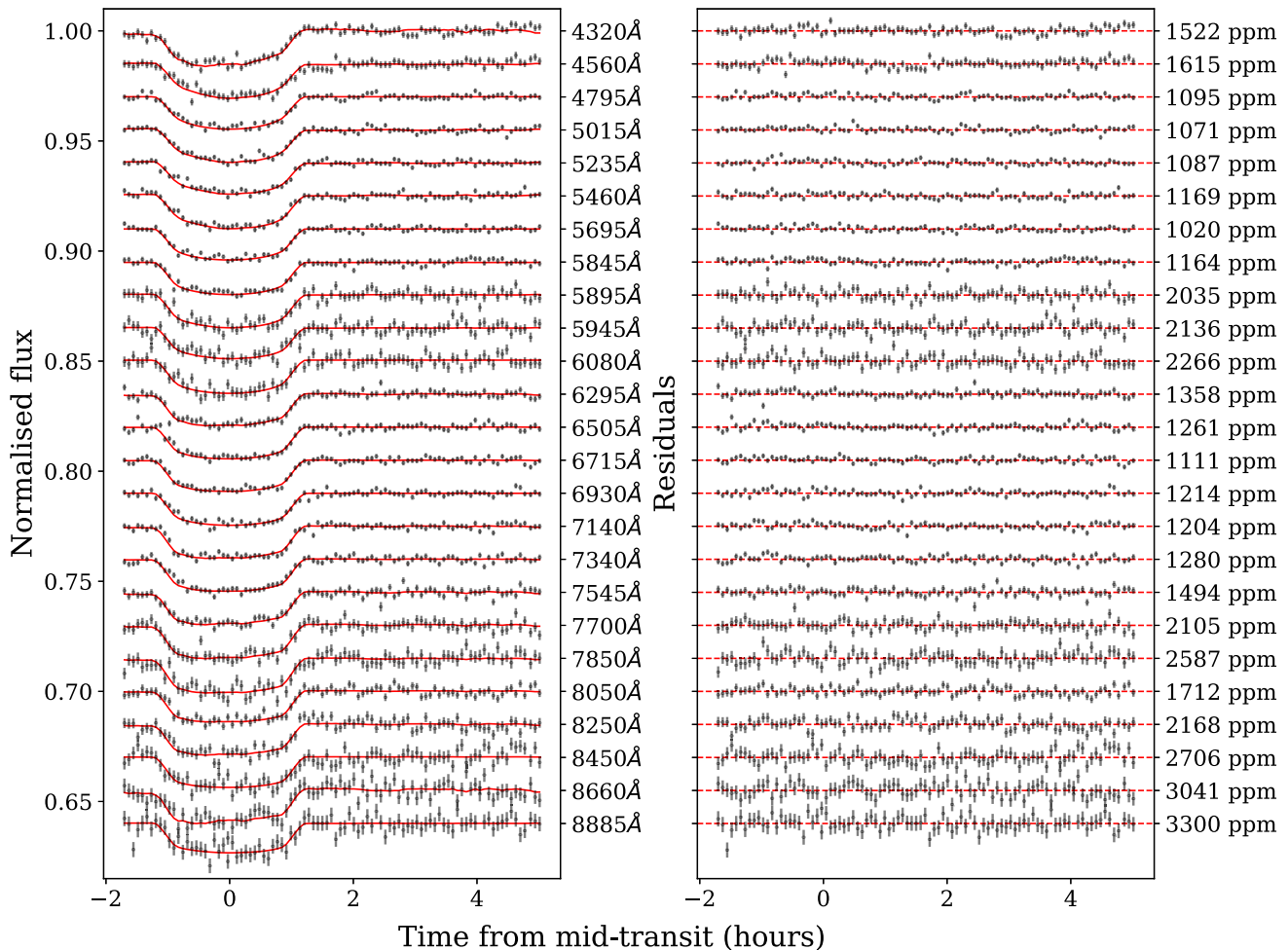


**Figure 4.** Left: Our fits (red) of the undetrended spectroscopic light curves (black) using a transit model and a linear in FWHM for detrending to the data with their respective centre wavelengths (blue end at the top) displayed on the right vertical axis. Right: Residuals of the corresponding light-curve fitting. The scatter is quantified in the form of the RMS on the right vertical axis.

of our choice of noise modelling. Following the points made earlier about each detrending approach, we selected a simple polynomial model, ‘Linear in FWHM’, as the preferred detrending method. The final transmission spectrum in tabular form is displayed in Table 3. Note that, for our final spectrum we chose to dismiss the relatively large transit depth of the bin centred on the potassium doublet due to the high chance of it being affected by the nearby strong telluric signal ( $O_2$  A band). Other studies in the past have come to similar conclusions when probing for potassium absorption with ground-based instruments (e.g. Kirk et al. 2017; McGruder et al. 2022).

#### 4.3 Atmospheric retrieval

We retrieve the transmission spectrum of HATS-46 b using the HYDRA (Gandhi & Madhusudhan 2018) and AURORA (Welbanks & Madhusudhan 2021) atmospheric retrieval codes. Our model uses 14 free parameters which describe the atmospheric composition, thermal profile, and cloud/haze properties (shown in Table 4) to generate spectra of HATS-46 b to compare against the observations. We use high temperature molecular line lists to compute the cross-sections and hence opacity for the spectrally active species, utilising the Kurucz line list for the atomic species Na and K (Kurucz & Bell 1995), and the ExoMol POKAZATEL line list for  $H_2O$  (Tennyson

et al. 2016; Polyansky et al. 2018). We spectrally broaden each line in the line list with both pressure and temperature, resulting in a Voigt profile (see e.g. Gandhi et al. 2020). We also include collisionally induced absorption from  $H_2-H_2$  and  $H_2-He$  interactions (Richard et al. 2012), as well as Rayleigh scattering due to  $H_2$ .

In addition to these sources of opacity, we also include four free parameters to model and fit for a partially cloudy and/or hazy atmosphere, as any clouds/hazes can have a strong influence on the overall spectrum. We include a grey (wavelength independent) cloud deck,  $P_{cl}$ , and two parameters that determine a wavelength-dependent haze, with  $\alpha_{haze}$  the strength and  $\gamma_{haze}$  the wavelength dependence of the haze (see e.g. Pinhas et al. 2018). Finally, we include the cloud/haze fraction,  $\phi_{cl}$ , as a free parameter, with the prior ranging from 0, representing a clear atmosphere, to 1, a fully cloudy/hazy atmosphere (see Table 4).

We model the temperature profile of the atmosphere using the method described in Madhusudhan & Seager (2009). This parametrization breaks the atmosphere into three distinct layers, with the temperature at the top of the model atmosphere included as a free parameter. We also retrieve the transition pressures  $P_1$  between the top layers 1 and 2 and  $P_3$  between layers 2 and 3. The top two layers have temperature-pressure gradients  $\alpha_1$  and  $\alpha_2$  as free parameters. The final deepest layer of the atmosphere is fixed to an isotherm,

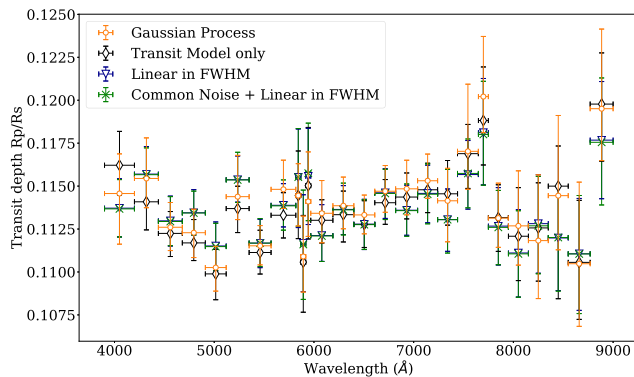


**Figure 5.** Transmission spectra of HATS-46 b using NTT/EFOSC2 observations. Median precisions of transit depths for  $\sim 200 \text{ \AA}$  wide bins are quoted in brackets in the description, respectively. The orange and blue colours represent the resulting transmission spectrum using GP (387 ppm) and a linear in FWHM (357 ppm) to account for systematics modelling, respectively. The black represents the case for when not using any noise modelling i.e. solely a transit model (326 ppm). The green indicates a model where the GP component fitted to the white-light light curve was subtracted (common noise model) from the spectroscopic light curves and then a linear in FWHM was used to fit residual systematics (358 ppm). The ‘linear in FWHM’ transmission spectrum is used for the retrieval analysis (see text for further details), but note that the bin centred on the potassium doublet (7665, 7699  $\text{\AA}$ ) is not included as it is affected by the closeby strong telluric O<sub>2</sub> line.

and continuity of the temperature between these layers results in six free parameters for the temperature profile. We restrict our parametrization to only allow non-inverted or isothermal temperature profiles given that we do not expect stratospheres for planets with

**Table 4.** Parameters and uniform prior ranges for our retrieval. We retrieve the Na, K, and H<sub>2</sub>O abundances, temperature profile, and partial cloud/haze parameters. Our temperature profile includes six free parameters, and our cloud/haze parametrization includes four free parameters (see Section 4.3).

| Parameter                            | Prior range            | Retrieval constraint    |
|--------------------------------------|------------------------|-------------------------|
| $\log(X_{\text{H}_2\text{O}})$       | $-15 \rightarrow -1$   | $-8.4^{+4.8}_{-4.2}$    |
| $\log(X_{\text{Na}})$                | $-15 \rightarrow -1$   | $-10.1^{+3.5}_{-3.0}$   |
| $\log(X_{\text{K}})$                 | $-15 \rightarrow -1$   | $-8.6^{+3.3}_{-4.0}$    |
| $T_{\text{top}}/\text{K}$            | $750 \rightarrow 2500$ | $1167^{+530}_{-300}$    |
| $\alpha_1 / \text{K}^{-\frac{1}{2}}$ | $0 \rightarrow 1$      | $0.67^{+0.21}_{-0.23}$  |
| $\alpha_2 / \text{K}^{-\frac{1}{2}}$ | $0 \rightarrow 1$      | $0.61^{+0.25}_{-0.27}$  |
| $\log(P_1/\text{bar})$               | $-6 \rightarrow 2$     | $-1.7 \pm 1.7$          |
| $\log(P_2/\text{bar})$               | $-6 \rightarrow 2$     | $-4.1^{+1.6}_{-1.3}$    |
| $\log(P_3/\text{bar})$               | $-2 \rightarrow 2$     | $0.60^{+0.90}_{-1.35}$  |
| $\log(P_{\text{ref}}/\text{bar})$    | $-4 \rightarrow 2$     | $-2.51^{+1.02}_{-0.86}$ |
| $\log(\alpha_{\text{haze}})$         | $-4 \rightarrow 6$     | $-0.0^{+2.8}_{-2.5}$    |
| $\gamma_{\text{haze}}$               | $-20 \rightarrow -1$   | $-11.3^{+6.3}_{-5.5}$   |
| $\log(P_{\text{cl}}/\text{bar})$     | $-6 \rightarrow 2$     | $-4.42^{+1.24}_{-0.94}$ |
| $\phi_{\text{cl}}$                   | $0 \rightarrow 1$      | $0.79^{+0.13}_{-0.19}$  |

such temperatures (e.g. Fortney et al. 2008), similar to previous work with transmission retrievals (e.g. Pinhas et al. 2019). We also include an additional free parameter for the reference pressure,  $P_{\text{ref}}$ , the point in the atmosphere where the radius of the planet is set. We model the atmosphere between 100 and  $10^{-6}$  bar with 100 layers evenly spaced in log pressure, and model the spectrum with 4000 wavelength points between 0.39 and 0.9  $\mu\text{m}$ . Our Bayesian analysis is carried out using the Nested Sampling algorithm MULTINEST (Feroz & Hobson 2008; Feroz, Hobson & Bridges 2009; Buchner et al. 2014).

**Table 3.** Retrieved transmission spectrum of HATS-46 b in tabulated form using the ‘linear in FWHM’ detrending approach, as plotted in Fig. 5, excluding the bin centred on the K doublet.

| Bins ( $\text{\AA}$ ) | $R_p/R_*$                    | u1              | u2 (fixed) |
|-----------------------|------------------------------|-----------------|------------|
| 3900–4200             | $0.1137^{+0.0018}_{-0.0017}$ | $0.92 \pm 0.02$ | $-0.0737$  |
| 4200–4440             | $0.1157 \pm 0.0017$          | $0.87 \pm 0.02$ | $-0.0523$  |
| 4420–4680             | $0.1130 \pm 0.0015$          | $0.79 \pm 0.02$ | $0.0380$   |
| 4680–4910             | $0.1134^{+0.0014}_{-0.0013}$ | $0.73 \pm 0.02$ | $0.0726$   |
| 4910–5120             | $0.1115^{+0.0014}_{-0.0015}$ | $0.71 \pm 0.02$ | $0.0721$   |
| 5120–5350             | $0.1154 \pm 0.0014$          | $0.67 \pm 0.02$ | $0.0837$   |
| 5350–5570             | $0.1117^{+0.0014}_{-0.0015}$ | $0.63 \pm 0.01$ | $0.1050$   |
| 5570–5818             | $0.1139 \pm 0.0013$          | $0.59 \pm 0.01$ | $0.1241$   |
| 5818–5868             | $0.1155^{+0.0029}_{-0.0030}$ | $0.58 \pm 0.01$ | $0.1330$   |
| 5868–5918             | $0.1117 \pm 0.0029$          | $0.58 \pm 0.01$ | $0.1209$   |
| 5918–5968             | $0.1156^{+0.0028}_{-0.0029}$ | $0.58 \pm 0.01$ | $0.1295$   |
| 5968–6190             | $0.1121^{+0.0018}_{-0.0016}$ | $0.55 \pm 0.01$ | $0.1336$   |
| 6190–6400             | $0.1136^{+0.0014}_{-0.0015}$ | $0.53 \pm 0.01$ | $0.1364$   |
| 6400–6610             | $0.1128 \pm 0.0015$          | $0.50 \pm 0.01$ | $0.1512$   |
| 6610–6820             | $0.1146 \pm 0.0015$          | $0.50 \pm 0.01$ | $0.1433$   |
| 6820–7040             | $0.1136 \pm 0.0015$          | $0.48 \pm 0.01$ | $0.1446$   |
| 7040–7240             | $0.1146^{+0.0017}_{-0.0018}$ | $0.47 \pm 0.01$ | $0.1449$   |
| 7240–7440             | $0.1130^{+0.0018}_{-0.0019}$ | $0.45 \pm 0.01$ | $0.1452$   |
| 7440–7649             | $0.1157^{+0.0020}_{-0.0021}$ | $0.44 \pm 0.01$ | $0.1464$   |
| 7749–7950             | $0.1127 \pm 0.0023$          | $0.42 \pm 0.01$ | $0.147$    |
| 7950–8150             | $0.1111 \pm 0.0026$          | $0.42 \pm 0.01$ | $0.1476$   |
| 8150–8350             | $0.1128 \pm 0.0029$          | $0.40 \pm 0.01$ | $0.1482$   |
| 8350–8550             | $0.1120^{+0.0030}_{-0.0031}$ | $0.38 \pm 0.01$ | $0.1474$   |
| 8550–8770             | $0.1111 \pm 0.0033$          | $0.37 \pm 0.01$ | $0.1488$   |
| 8770–9000             | $0.1177 \pm 0.0035$          | $0.37 \pm 0.01$ | $0.1494$   |

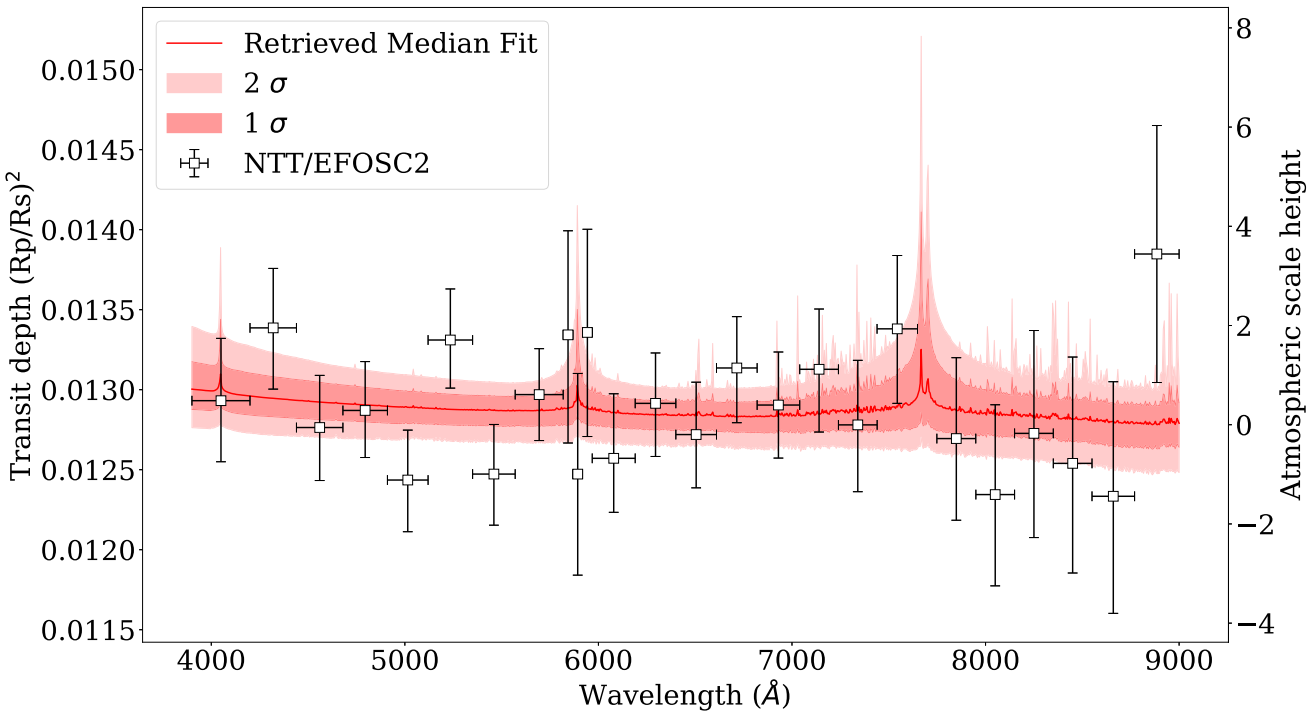


**Figure 6.** Transmission spectrum of HATS-46 b as observed by NTT/EFOSC2 and using linear in FWHM detrending (black), and the median retrieved atmospheric model (red), including the respective  $1\sigma$  and  $2\sigma$  confidence intervals. It is shown that the retrieved transmission spectrum is relatively featureless, suggesting high-altitude clouds in the atmosphere. Note that, narrower bins around the Na doublet ( $5890, 5895 \text{ \AA}$ ) are used to probe for absorption and the bin centred on the K doublet ( $7665, 7699 \text{ \AA}$ ) was disregarded due to the close strong  $\text{O}_2$  telluric line.

The best-fit retrieval and retrieved constraints are shown in Fig. 6 and Table 4, and the posterior distribution is shown in Fig. A1. For our retrievals, we considered two competing scenarios: a cloudy/hazy atmosphere and a relatively clear atmosphere. The first case, where clouds mask atomic and molecular species in the transmission spectrum of HATS-46 b, is statistically preferred to  $3.0\sigma$  due to the relatively featureless spectrum, when using Bayesian model evidence comparisons (e.g. Benneke & Seager 2013; Welbanks & Madhusudhan 2021). In the alternative, less statistically preferred scenario of a clear atmosphere, where clouds do not mask the atomic and molecular species, we can place constraints on the abundance of K and Na. There is no visible feature of Na in the spectrum; hence we place an upper limit on Na abundance of  $\log(\text{Na}) < -4.45$  to  $3\sigma$ , i.e. less than  $20\times$  solar Na abundance for this cloud-free scenario. This is a conservative upper limit, since the lack of features in the transmission spectrum drives the atmospheric temperatures in the model to the lower end of the prior, which decreases the atmospheric scale height and thereby the strength of features. There is therefore a degeneracy between temperature and abundance, and an atmospheric temperature closer to the equilibrium temperature would give a tighter limit on abundance.

Additionally, we assess the impact of unocculted star-spots and faculae in the transmission spectrum of HATS-46 b using AURORA (Welbanks & Madhusudhan 2021). We allow for the possibility of a contaminated stellar photosphere and retrieve for three additional parameters to the fiducial model described earlier. These are the photospheric temperature (Gaussian prior centred at effective temperature of the star and a width of 100 K), the fraction of unocculted spots or faculae (uniform prior between 0 and 50 per cent), and the temperature of these inhomogeneities (uniform prior from 0.5 to 1.5 times the effective temperature of the star). Priors are in line with

what is recommended by Pinhas et al. (2018). The retrieved stellar properties are in agreement with the possibility of a spotless star. The retrieved photospheric temperature of HATS-46 is consistent with the reported value in Table 1, with a relatively low fraction of spots (i.e.  $2\sigma$  upper limit of  $\lesssim 22$  per cent) with temperatures consistent with the photospheric stellar temperature at  $2\sigma$ . The presence of stellar heterogeneities is not preferred since its Bayesian evidence value is lower relative to our fiducial model. Based on these observations and the models considered here, we find no evidence for stellar contamination affecting our observations.

## 5 DISCUSSION AND CONCLUSIONS

We presented the analysis and results of spectroscopic NTT/EFOSC2 data of HATS-46 b in transmission. The inflated, Jupiter-sized exoplanet orbits its relatively faint ( $V_{\text{mag}} = 13.6$ ) G-type host star in a 4.7-d period and has an equilibrium temperature of 1100 K (Louden & Hartman 2021).

One transit was observed with NTT/EFOSC2 using the method of long-slit spectroscopy and a comparison star was used to conduct differential spectroscopy. A total of 93 spectral frames with exposure times of 240 s were acquired. The resulting light curves did not show noise structures beyond a weak dependence on seeing, with fitted average amplitudes of 600 ppm for our best noise model, which included a linear detrend against FWHM.

We extracted the transmission spectrum in 26 bins, covering the wavelength range of 3900–9000 Å with a median transit depth uncertainty of 357 ppm for the  $\sim 200 \text{ \AA}$ -wide bins. The measured transmission spectrum is relatively featureless; it does not show a sodium feature or a scattering slope. The fitted, relatively large transit depth at the wavelength of the potassium doublet was dismissed as

an effect of the nearby strong telluric signal due to the O<sub>2</sub> A band. Our atmospheric retrieval analysis of the transmission spectrum of HATS-46 b favours a cloudy atmosphere with  $3.0\sigma$  confidence. In an alternative cloud-free model we place a conservative upper limit on the Na abundance of  $20\times$  solar ( $3\sigma$  confidence). Including stellar activity in our retrievals results in lower Bayesian evidence and no meaningful constraints on the additional parameters. If activity were to play a role in the shape in our transmission spectrum, we would expect to retrieve constraints on the spot coverage fraction or temperature of the spots. Thus, the cloudy atmosphere model without the additional stellar activity parameters is favoured.

## ACKNOWLEDGEMENTS

This research has made use of the NASA Exoplanet Archive, which is operated by the California Institute of Technology, under contract with the National Aeronautics and Space Administration under the Exoplanet Exploration Program. PJW acknowledges support from the Science and Technology Facilities Council (STFC) under consolidated grant nos ST/P000495/1 and ST/T000406/1. SG is grateful to Leiden Observatory at Leiden University for the award of the Oort Fellowship. JK acknowledges financial support from Imperial College London through an Imperial College Research Fellowship grant.

## DATA AVAILABILITY

The raw data used in our analysis are available from the ESO data archive under ESO programme 099.C-0390(A) (PI: Kirk). The reduced light curves presented in this article will be available via VizieR at CDS (Ochsenbein, Bauer & Marcout 2000).

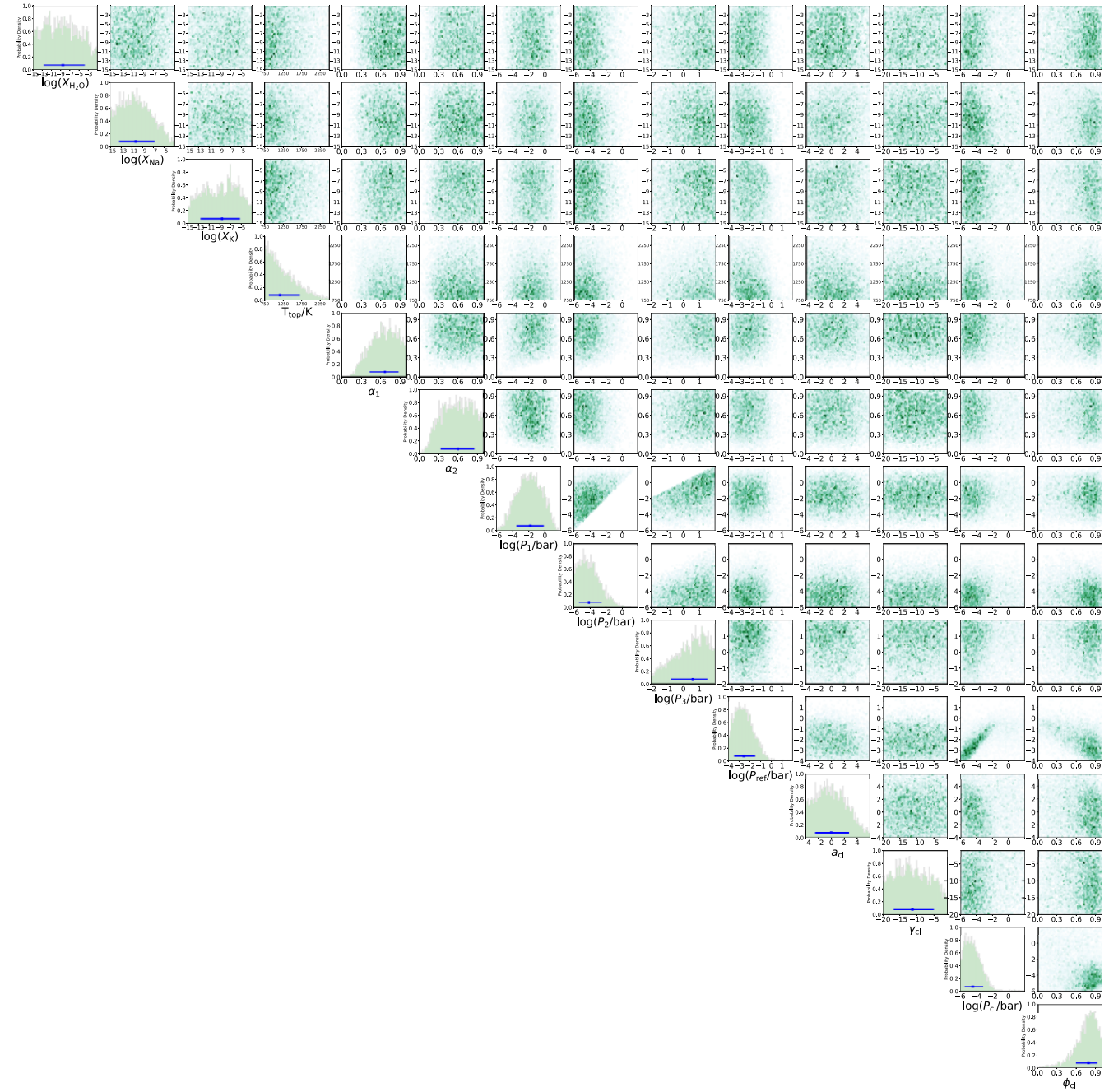
## REFERENCES

- Ahrer E., Wheatley P. J., Kirk J., Gandhi S., King G. W., Louden T., 2022, *MNRAS*, 510, 4857
- Ahrer E.-M. et al., 2023, *Nature*, 614, 653
- Alam M. K. et al., 2021, *ApJ*, 906, L10
- Alam M. K. et al., 2022, *ApJ*, 927, L5
- Alderson L. et al., 2020, *MNRAS*, 497, 5182
- Alderson L. et al., 2023, *Nature*, 614, 664
- Bakos J. A. et al., 2013, *PASP*, 125, 154
- Bean J. L., Kempton E. M. R., Homeier D., 2010, *Nature*, 468, 669
- Benneke B., Seager S., 2013, *ApJ*, 778, 153
- Bixel A. et al., 2019, *AJ*, 157, 68
- Booth R. A., Clarke C. J., Madhusudhan N., Ilee J. D., 2017, *MNRAS*, 469, 3994
- Brahm R. et al., 2018, *AJ*, 155, 112
- Buchner J. et al., 2014, *A&A*, 564, A125
- Buzzoni B. et al., 1984, *The Messenger*, 38, 9
- Carter A. L. et al., *MNRAS*, 494, 5449
- Charbonneau D., Brown T. M., Noyes R. W., Gilliland R. L., 2002, *ApJ*, 568, 377
- Chen G. et al., 2021, *MNRAS*, 500, 5420
- Espinoza N. et al., 2019, *MNRAS*, 482, 2065
- Feinstein A. D. et al., 2023, *Nature*, 614, 670
- Feroz F., Hobson M. P., 2008, *MNRAS*, 384, 449
- Feroz F., Hobson M. P., Bridges M., 2009, *MNRAS*, 398, 1601
- Fischer P. D. et al., 2016, *ApJ*, 827, 19
- Fisher C., Heng K., 2018, *MNRAS*, 481, 4698
- Fortney J. J., Lodders K., Marley M. S., Freedman R. S., Fortney J. J., Lodders K., Marley M. S., Freedman R. S., 2008, *ApJ*, 678, 1419
- Fu G., Deming D., Knutson H., Madhusudhan N., Mandell A., Fraine J., 2017, *ApJ*, 847, L22
- Gandhi S., Madhusudhan N., 2018, *MNRAS*, 474, 271
- Gandhi S. et al., 2020, *MNRAS*, 495, 224
- Gao P. et al., 2020, *Nat. Astron.*, 4, 951
- Gibson N. P., Aigrain S., Barstow J. K., Evans T. M., Fletcher L. N., Irwin P. G., 2013a, *MNRAS*, 428, 3680
- Gibson N. P., Aigrain S., Barstow J. K., Evans T. M., Fletcher L. N., Irwin P. G., 2013b, *MNRAS*, 436, 2974
- Handley W. J., Hobson M. P., Lasenby A. N., 2015, *MNRAS*, 453, 4384
- Heng K., 2016, *ApJ*, 826, L16
- Huitson C. M., Désert J.-M., Bean J. L., Fortney J. J., Stevenson K. B., Bergmann M., 2017, *AJ*, 154, 95
- Husser T. O., Wende-Von Berg S., Dreizler S., Homeier D., Reiners A., Barman T., Hauschildt P. H., 2013, *A&A*, 553, A6
- Kipping D. M., 2013, *MNRAS*, 435, 2152
- Kirk J., Wheatley P. J., Louden T., Littlefair S. P., Copperwheat C. M., Armstrong D. J., Marsh T. R., Dhillon V. S., 2016, *MNRAS*, 463, 2922
- Kirk J., Wheatley P. J., Louden T., Doyle A. P., Skillen I., McCormac J., Irwin P. G. J., Karjalainen R., 2017, *MNRAS*, 468, 3907
- Kirk J., Wheatley P. J., Louden T., Skillen I., King G. W., McCormac J., Irwin P. G., 2018, *MNRAS*, 474, 876
- Kirk J., López-Morales M., Wheatley P. J., Weaver I. C., Skillen I., Louden T., McCormac J., Espinoza N., 2019, *AJ*, 158, 144
- Kirk J. et al., 2021, *AJ*, 162, 34
- Knutson H. A., Benneke B., Deming D., Homeier D., 2014, *Nature*, 505, 66
- Kreidberg L., 2015, *PASP*, 127, 1161
- Kreidberg L. et al., 2014, *Nature*, 505, 69
- Kurucz R. L., Bell B., 1995, Atomic Line Data. Smithsonian Astrophysical Observatory, Cambridge, MA
- Lendl M. et al., 2016, *A&A*, 587, A67
- Lendl M., Cubillos P. E., Hagelberg J., Müller A., Juvan I., Fossati L., 2017, *A&A*, 606, A18
- Louden E. M., Hartman J. D., 2021, *MNRAS*, 501, 5393
- Louden T., Wheatley P. J., Irwin P. G. J., Kirk J., Skillen I., 2017, *MNRAS*, 470, 742
- McGruder C. D. et al., 2022, *AJ*, 164, 134
- Madhusudhan N., Seager S., 2009, *ApJ*, 707, 24
- Madhusudhan N., Amin M. A., Kennedy G. M., 2014, *ApJ*, 794, L12
- Mandel K., Agol E., 2002, *ApJ*, 580, L171
- May E. M., Zhao M., Haidar M., Rauscher E., Monnier J. D., 2018, *AJ*, 156, 122
- Nikolov N., Sing D. K., Gibson N. P., Fortney J. J., Evans T. M., Barstow J. K., Kataria T., Wilson P. A., 2016, *ApJ*, 832, 191
- Nikolov N. et al., 2018, *Nature*, 557, 526
- Nortmann L., Pallé E., Murgas F., Dreizler S., Iro N., Cabrera-Lavers A., 2016, *A&A*, 594, A65
- Öberg K. I., Murray-Clay R., Bergin E. A., 2011, *ApJ*, 743, L16
- Ochsenbein F., Bauer P., Marcout J., 2000, *A&AS*, 143, 23
- Parviainen H., Aigrain S., 2015, *MNRAS*, 453, 3821
- Pinhas A., Rackham B. V., Madhusudhan N., Apai D., 2018, *MNRAS*, 480, 5314
- Pinhas A., Madhusudhan N., Gandhi S., MacDonald R., 2019, *MNRAS*, 482, 1485
- Polyansky O. L., Kyuberis A. A., Zobov N. F., Tennyson J., Yurchenko S. N., Lodi L., 2018, *MNRAS*, 480, 2597
- Pont F., Sing D. K., Gibson N. P., Aigrain S., Henry G., Husnoo N., 2013, *MNRAS*, 432, 2917
- Rackham B. et al., 2017, *ApJ*, 834, 151
- Richard C. et al., 2012, *J. Quant. Spectrosc. Radiat. Transfer*, 113, 1276
- Rustamkulov Z. et al., 2023, *Nature*, 614, 659
- Sing D. K. et al., 2012, *MNRAS*, 426, 1663
- Sing D. K. et al., 2016, *Nature*, 529, 59
- Snellen I. A., Albrecht S., De Mooij E. J., Le Poole R. S., 2008, *A&A*, 487, 357
- Spyratos P. et al., 2021, *MNRAS*, 506, 2853
- Stevenson K. B., Bean J. L., Seifahrt A., Désert J. M., Madhusudhan N., Bergmann M., Kreidberg L., Homeier D., 2014, *AJ*, 147, 161
- Tennyson J. et al., 2016, *J. Mol. Spectrosc.*, 327, 73

- The JWST Transiting Exoplanet Community Early Release Science Team, 2022, *Nature*, 614, 649  
 Todorov K. O. et al., 2019, *A&A*, 631, A169  
 Veitch-Michaelis J., Lam M. C., 2019, in Pizzo R., Deul E. R., Mol J. D., de Plaa J., Verkouter H., eds, ASP Conf. Ser. Vol. 202, Astronomical Data Analysis Software and Systems XXIX. Astron. Soc. Pac., San Francisco, p. 627  
 Weaver I. C. et al., 2020, *AJ*, 159, 13

- Weaver I. C. et al., 2021, *AJ*, 161, 278  
 Welbanks L., Madhusudhan N., 2021, *ApJ*, 913, 114  
 Wilson J. et al., 2020, *MNRAS*, 497, 5155

## APPENDIX: POSTERIOR DISTRIBUTIONS



Downloaded from <https://academic.oup.com/mnras/article/521/4/5636/7030153> by guest on 22 August 2023

**Figure A1.** Posterior distribution of HATS-46 b from the retrieval of the NTT/EFOSC2 observations of HATS-46 b. We retrieved three chemical species,  $\text{H}_2\text{O}$ , Na, and K, and parametrized the atmospheric temperature profile with six parameters, as discussed in Section 4.3. We also include additional parameters for the reference pressure and partial clouds/hazes.

This paper has been typeset from a  $\text{\TeX}/\text{\LaTeX}$  file prepared by the author.